

OPEN ACCESS

Corrosion Behaviour of Electron Beam Melted Ti6Al4V: Effects of Microstructural Variation

To cite this article: V. Dehnavi *et al* 2020 *J. Electrochem. Soc.* **167** 131505

View the [article online](#) for updates and enhancements.

Discover the EL-CELL potentiostats

- Fully independent test channels with Pstat / GStat / EIS
- Optionally with integrated temperature controlled cell chamber
- Unique Connection Matrix: Switch between full-cell and half-cell control at runtime

www.el-cell.com +49 (0) 40 79012 734 sales@el-cell.com





Corrosion Behaviour of Electron Beam Melted Ti6Al4V: Effects of Microstructural Variation

V. Dehnavi,^{1,2,z} J. D. Henderson,^{2,*} C. Dharmendra,³ B. S. Amirkhiz,^{3,4} D. W. Shoosmith,^{1,2,**} J. J. Noël,^{2,***} and M. Mohammadi³

¹Surface Science Western, Western University, London, ON N6G 0J3, Canada

²Department of Chemistry, Western University, London, ON N6A 5B7, Canada

³Marine Additive Manufacturing Centre of Excellence (MAMCE), University of New Brunswick, Fredericton, NB E3B 5A1, Canada

⁴CanmetMATERIALS, Natural Resources Canada, Hamilton, ON L8P 0A5, Canada

Microstructural analysis and electrochemical measurements were carried out on longitudinal and transverse planes of an additively manufactured (AM) Ti-6Al-4V rod printed in the horizontal direction by electron beam melting (EBM), and compared with those performed on a commercially available alloy. Microstructural differences in the planes parallel and perpendicular to the build direction were characterized using optical and scanning electron microscopy, X-ray diffraction, and transmission electron microscopy coupled with energy dispersive spectroscopy. The microstructures of three different locations along the transverse axis on the EBM samples were also studied. The starting point, the middle, and the end of the sample in the build direction consisted primarily of α -phase and a small amount of β -phase. On progressing from the starting point towards the end of the build, the size of both phases increased and the elemental distribution of alloying elements showed more segregation of vanadium and iron into the β -phase. The electrochemical behaviour was studied as a function of time using electrochemical impedance spectroscopy and potentiodynamic polarization. The film resistance of the wrought sample was slightly better than those of the EBM samples. The film resistance of the EBM-transverse sample improved slightly more with exposure time than that of the longitudinal sample. © 2020 The Author(s). Published on behalf of The Electrochemical Society by IOP Publishing Limited. This is an open access article distributed under the terms of the Creative Commons Attribution Non-Commercial No Derivatives 4.0 License (CC BY-NC-ND, <http://creativecommons.org/licenses/by-nc-nd/4.0/>), which permits non-commercial reuse, distribution, and reproduction in any medium, provided the original work is not changed in any way and is properly cited. For permission for commercial reuse, please email: permissions@iopublishing.org. [DOI: 10.1149/1945-7111/abb9d1]



Manuscript submitted July 22, 2020; revised manuscript received September 17, 2020. Published September 28, 2020.

Additive manufacturing (AM) processes have gained increasing attention over the past few years due to their unique features to fabricate complex, three-dimensional, and near-net-shape parts as compared to conventional manufacturing processes. AM facilitates direct fabrication of intricate, or customized parts through a layer-by-layer deposition approach that eliminates the intermediate steps commonly required in conventional materials processing methods.^{1,2} The high material utilization efficiency of the AM process, combined with geometric freedom can provide considerable cost savings.³

A number of different metal AM processes are currently available and can be categorized based on the heat source (arc, laser, electron beam) and how the material is supplied (powder or wire feed).⁴ However, two metal AM techniques have recently received much scientific attention: powder bed fusion processes, including selective laser melting (SLM) and electron beam melting (EBM); and direct laser deposition (DLD), also known as direct energy deposition (DED). In powder bed fusion processes, parts are manufactured layer-by-layer in a powder bed by rastering a high-power source of energy. However, in direct laser deposition, metallic wires are used as feedstock and the energy is electrically supplied.²

Ti-6Al-4V (Ti64) is the most popular and widely used titanium alloy, providing approximately half of the global market share of titanium products mainly due to its low density, high strength and fracture toughness, excellent corrosion resistance, and superior biocompatibility.^{5,6} Titanium and its alloys have proven to be invaluable in many industries, in particular the aerospace industry, which uses about 80% of total titanium production.⁷ Ti64 comprises about 85% of the total volume of titanium alloys used in airframe components and 60% of the titanium used in jet engine parts.⁸

Ti64 components have been conventionally fabricated by casting, forging, extrusion, and powder metallurgy manufacturing processes. These conventional methods involve multiple processing steps that

are time-consuming and incapable of readily producing complex shapes with the required mechanical properties at a reasonable cost. In addition, Ti64 is classified as a difficult metal to machine and weld compared to other common industrial metals and alloys, resulting in further increases in production costs when using conventional methods.^{6,9,10} By contrast, AM techniques offer greater freedom of design enabling manufacturers to produce Ti64 complex parts more efficiently.^{6,11} These advantages and unique features of AM technologies have challenged conventional approaches to design and maintenance, especially in aerospace and biomedical applications.^{2,11}

Most studies to date on Ti64 produced by AM have focused on the mechanical properties and, based on the available literature, the mechanical properties of samples produced by AM have been shown to be better than their conventionally processed counterparts.^{1,5,12,13} While aerospace applications place great importance on mechanical properties, industrial applications also require a thorough understanding of corrosion performance. The structural and mechanical properties of Ti64 samples manufactured by SLM and EBM methods have been extensively discussed in the literature,^{12,14–19} but the study of their corrosion performance remains in its infancy² and critically sought after for applications in naval and aviation structures.²⁰

The microstructure and composition of Ti alloys can play a significant role in determining their corrosion performance. Ti64 is a dual-phase alloy comprised of an alpha (α) phase, with a hexagonal close-packed (HCP) structure, stabilized by Al, and a beta (β) phase, with a body-centred cubic (BCC) phase, stabilized by V. Irrespective of alloy composition, corrosion resistance is attributable to the presence of a chemically inert, adherent TiO₂ film, which, in Ti64, can be slightly enriched in both Al and V.^{21,22} The presence of oxygen vacancies (O_v) and Ti(III) interstitial ions makes the film an n-type semiconductor. The presence and distribution of Fe (generally <0.2 wt% in Ti) can lead to a decrease in α -grain size and the stabilization of the β -phase, as well as the precipitation of Ti_xFe intermetallic particles along grain boundaries and at triple points.²³ The oxide can be anatase or rutile^{24,25} and anodic polarization leads to thickening of the oxide and a decrease in the number density of

*Electrochemical Society Student Member.

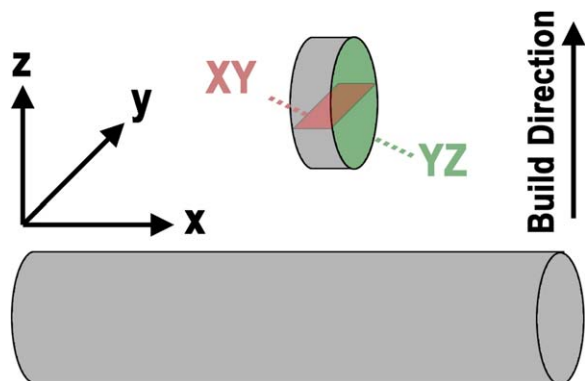
**Electrochemical Society Fellow.

***Electrochemical Society Member.

^zE-mail: vdehnavi@uwo.ca

Table I. Nominal chemical composition (in weight %) of a typical Ti64 powder.

Al	V	Fe	O	C	N	H	Ti
6	4	0.1	0.15	0.03	0.01	0.003	Balance

**Figure 1.** Graphical representation of the as-printed EBM Ti64 rod. The examined cross-sections are indicated by the green (YZ) and red (XY) planes.

defects.^{24,26} The film at grain boundaries may be less protective than that on the grains.²⁷

The microstructures of AM produced parts are significantly different from their conventionally-produced counterparts due to various AM process variables.² AM is a relatively rapid solidification process and the heat flow during AM is directional which, in most cases, results in columnar microstructures.³ Limited studies of the corrosion performance of AM manufactured Ti64 parts have been published. Dai et al.^{28,29} examined the corrosion performance of Ti64 samples prepared by SLM and observed variations in the corrosion performance of different planes with respect to the build direction. They also reported that parts manufactured by AM showed an inferior corrosion resistance compared to commercial-grade Ti64 samples. The inferior corrosion resistance on the plane parallel to the build direction was attributed to the presence of a higher α' martensite and a lower amount of β -phase.

Post heat-treatment is typically required for SLM-fabricated Ti64 parts to transform acicular α' martensite into β -phase. Although the cooling rates produced in the EBM process are similar (10^3 – 10^5 K s⁻¹) to that of the rates in SLM and DED processes, the thermal behaviour of the EBM-Ti64 part is very different since a high temperature (600 °C to 750 °C) is maintained in the powder bed. This high build temperature is analogous to the post-heat treatment process, which is sufficient to fully decompose and transform any α' martensite into $\alpha + \beta$. EBM process also operates under vacuum and minimizes oxygen pick up. These differences in the features between SLM and EBM produce markedly different microstructures.^{1–3}

Despite these advantages in the as-built condition, unfortunately, the corrosion behaviour of EBM-Ti64 has received very minimal attention thus far. In a recent study, the electrochemical behaviour of EBM-produced Ti64 samples was compared with their wrought counterparts in a buffered saline solution.²⁹ It was found that the EBM-Ti64 exhibited marginally better corrosion resistance than the

wrought Ti64 alloy due to the larger proportions of β -phase and ultrafine-grained lamellar α/β in the EBM microstructure. However, the authors did not mention which plane on the EBM samples was chosen for corrosion tests.

The available literature comparing the corrosion performance of EBM produced and wrought samples has many shortcomings. In most research studies the corrosion performance is not examined over time resulting in limited available information on the evolution of corrosion behaviour with time. In addition, it is typically not clear whether the samples were exposed to air for the same amount of time after polishing and before performing corrosion experiments. This is important since all freshly polished Ti alloys develop an air-formed surface oxide whose protective properties change with time, which can influence the subsequent test results.

The objective of the present work is to study the microstructural variation along the build direction of a horizontally printed EBM-Ti64 rod, correlate the microstructural differences in the longitudinal and transverse planes with the difference in the corrosion behaviour of EBM-Ti64, and compare the results with the corrosion behaviour of commercial wrought Ti64 alloy. The evolution of corrosion performance with time is studied with extra attention paid to making sure the preparation of samples and their exposure prior to experiments were identical.

Experimental

Sample fabrication and preparation.—The samples used in this study were additively manufactured from a Ti64 powder using an Arcam Q10 electron beam melting (EBM) system with a stainless steel building plate of 200 mm × 200 mm × 180 mm. The EBM system was comprised of a single crystalline cathode operating at a maximum beam power of 3000 W with the system under a vacuum of 5×10^{-4} mbar. The beam spot size was 450 to 500 μ m in diameter. The Ti64 powder with a particle size of 45–100 μ m was provided by Advanced Powders and Coatings Inc. (AP&C). The chemical composition of the powder in the as-received condition is listed in Table I.

Samples were fabricated in the form of rods with a diameter of 11 mm and a length of 120 mm in the horizontal direction, with their longitudinal direction (X) perpendicular to the build direction (Z), Fig. 1. The examined planes of the AM samples have been labelled in Fig. 1 and will be referred to as EBM-XY and EBM-YZ. The EBM process parameters employed to fabricate the samples were recommended by Arcam to minimize the final porosity in the samples. These parameters include a hatch distance of 0.2 mm, a layer orientation of 46°, a layer thickness of 50 μ m, and a bed temperature of 650 °C–700 °C. The maximum scan speeds in the contour and hatch were 800 mm s⁻¹, and 4500 mm s⁻¹, respectively.

The properties of the additively manufactured samples were compared with those of a wrought (hot rolled) Ti64 rod sample in the mill-annealed condition. The chemical composition, as reported by the manufacturer, is summarized in Table II.

Microstructural characterization.—Samples selected for metallographic examination were mechanically ground using silicon carbide papers and finally polished with a mixture of 0.04 μ m colloidal silica and hydrogen peroxide. They were then etched with Kroll's reagent (1 ml HF, 2 ml HNO₃, and 97 ml water) and examined with an optical microscope.

The microstructures of the as-built EBM and wrought samples were also analysed using a Hitachi SU3500 variable pressure scanning electron microscope (SEM) in combination with an

Table II. Chemical composition (in weight%) of the wrought Ti–6Al–4V sample.

Al	V	Fe	O	C	N	Y	Ti
6.38–6.39	4.02–4.09	0.16–0.17	0.15–0.17	0.03–0.04	0.02	<0.001	Balance

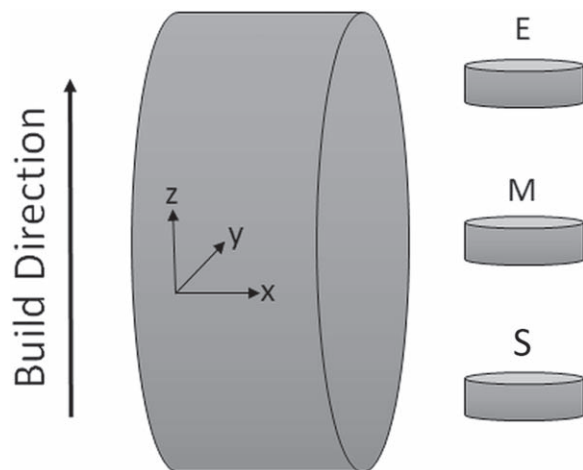


Figure 2. Graphical representation of the locations of the samples prepared for TEM. (S, the starting point, M, the middle, and E, the end of the build).

Oxford Aztec X-Max50 X-ray analyser. SEM examinations were performed on the as-polished samples in the back-scattered electron (BSE) mode.

The as-built microstructures of the EBM samples were studied in detail using an FEI Tecnai Osiris transmission electron microscope (TEM) equipped with a 200 keV X-FEG gun. The Super-EDS X-ray detection system combined with the high current density electron beam in the scanning mode (STEM) was also used to analyse the fine details of the microstructure. Spatial resolutions on the order of 1 nm were obtained during EDS elemental mapping using a sub-nanometer electron probe.

To prepare electron-transparent samples for TEM characterisation, a thin slice ($<500\ \mu\text{m}$) of the sample was cut using a diamond wafering blade. Then, three disks with diameters of 3 mm were punched from the starting point (S), the middle (M), and the end of the build (E), Fig. 2, using a Gatan puncher. The disks were then polished to a thickness of approximately $80\text{--}90\ \mu\text{m}$. Dimpling of the samples was performed by employing a $4\text{--}6\ \mu\text{m}$ CBN paste with a felt wheel and finished using an alumina suspension down to $\sim 10\ \mu\text{m}$ at the centre of the sample. The dimpled disks were finally ion milled until perforation was achieved with a Gatan 691 PIPS using liquid nitrogen cooling at 5, 3, and 1 keV and a gun angle of 4° for 130, 10 and 30 min average time at each step, respectively.

XRD analyses were performed using a Rigaku SmartLab X-ray diffraction system with $\text{CuK}\alpha$ radiation ($\lambda = 1.54059\ \text{\AA}$) in Bragg-Brentano geometry. A micro-area attachment was used to focus the X-ray on areas of interest on the samples. Diffraction data were acquired over a 2θ range from 30° to 90° with a step width of 0.02° . The ICDD PDF-4 + 2019 inorganic diffraction database was used for phase identification.

Electrochemical measurements.—Electrochemical measurements were carried out in a three-electrode glass cell with three compartments. The Pt counter electrode (CE) and the reference electrode (RE), a saturated calomel electrode (SCE), were housed in separate compartments isolated by porous glass frits. Prior to all experiments, the RE was calibrated against a “master” electrode, used only for verification tests. Measurements were made using either a Solartron 1287 or a Modulab XM MTS system. The cell was housed inside a Faraday cage to reduce electrical noise from external sources.

To ensure initial surface conditions were the same in all experiments, all samples were prepared using an identical procedure: Samples were successively ground using SiC abrasive papers up to P4000 followed by polishing with a mixture of $0.04\ \mu\text{m}$ colloidal silica and a 3% solution of hydrogen peroxide. Then they were sonicated in ethanol for 3.5 min and finally dried in a stream of Ar

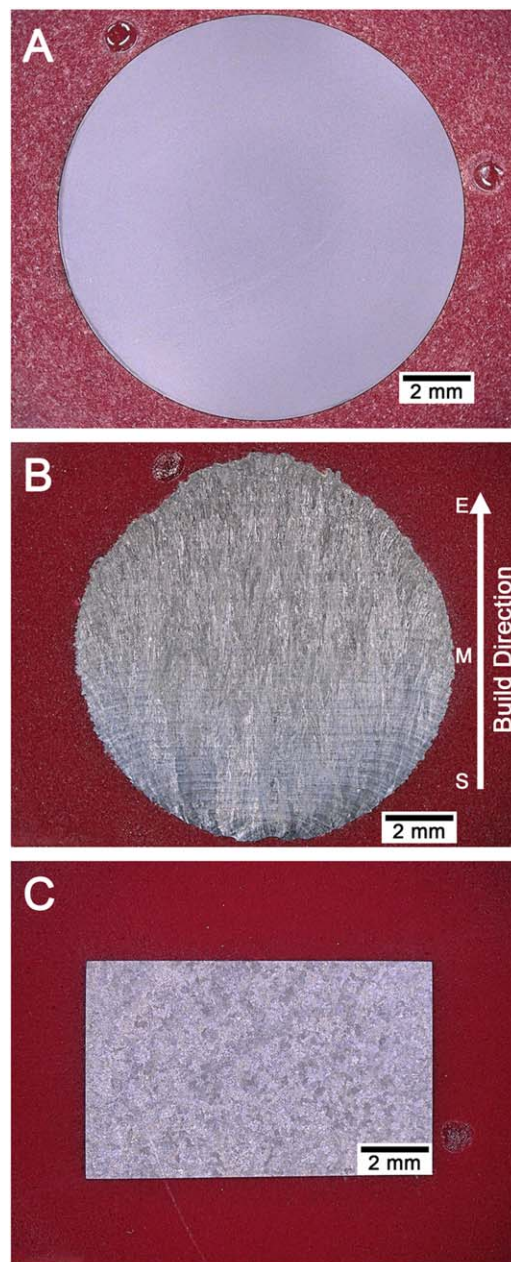


Figure 3. Macrostructures of etched (A) wrought Ti64, (B) EBM-YZ specimen, and (C) EBM-XY specimens. The build direction is indicated for the YZ plane, while the XY plane was taken from the middle (M) of the build.

gas. The samples were then exposed to air for 30 min before electrochemical measurements were conducted.

Corrosion behaviour was studied in a naturally aerated 3.5 wt.% NaCl solution at room temperature. Measurements involved monitoring the corrosion potential (E_{corr}) for 30 min, followed by electrochemical impedance spectroscopy (EIS) at 0.5, 2, 4, 8, and 12 h intervals, and finally potentiodynamic polarization (PDP) after 16 h of immersion. EIS spectra were obtained at E_{corr} using a sinusoidal input potential with an amplitude of 10 mV (vs E_{corr}) over a frequency range of 10^5 to 10^{-2} Hz. EIS data were analysed by fitting an appropriate electrical equivalent circuit to experimental data using ZView software (Scribner Associates). All electrochemical experiments were repeated at least three times to verify their reproducibility. PDP measurements were initiated at $-0.1\ \text{V}$ (vs

E_{corr}) and the potential scanned in the positive direction to 2.5 V (vs RE) at a scan rate of 10 mV min^{-1} .

Results and Discussion

Macro- and micro-structures.—Figure 3 shows optical images highlighting the macro-scale features found on the etched wrought sample (A) as well as the EBM-YZ (B) and EBM-XY (C) specimens with the relative locations of the YZ and XY planes shown in Fig. 1. For the EBM-YZ sample, Fig. 3B, the build direction is indicated with three positions labelled; the starting point (S), middle (M), and end (E) of the build. The EBM-XY sample, Fig. 3C was taken perpendicularly at approximately the middle (M) of the build. As a result of the AM process, which included high temperature, vacuum atmosphere, rapid solidification, and layer-by-layer deposition of the sample, and exposed the metal to several heating/cooling cycles, samples produced by EBM display microstructures very different from those of samples produced by traditional methods.¹³

While wrought samples were found to be relatively homogeneous, EBM samples exhibited two significant directional features. First, as shown in the EBM-YZ sample, Fig. 3B, a series of layers perpendicular to the build direction, a result of the layer-by-layer deposition, was apparent. The characteristics of these layers have been shown to be influenced by beam diameter, scan spacing, energy density, powder layer thickness, characteristics of the feedstock powder, etc.^{30,31} Secondly, grains demonstrated columnar growth, i.e., growing parallel to the build direction. As seen in Fig. 3B, features were elongated preferentially along the build direction. In the EBM-XY sample, Fig. 3C, these elongated grain structures were truncated, showing smaller, non-directional features on the macro-scale. This type of columnar solidification has been well documented and attributed to directional heat extraction, in this case along the build direction.^{32–34}

Representative SEM images for wrought Ti64, EBM-YZ at two different regions along the build direction, and EBM-XY are shown in Fig. 4. In BSE-SEM images, the contrast between the two phases arises from differences in the electron density, with the dark and

light areas being the α - and β -phases, respectively. In the case of wrought-Ti64, Fig. 4A, the microstructure was found to be relatively homogenous, the α -phase (dark areas) having an equiaxed (or globular) grain structure with β -phase (light areas) located on the phase boundaries. EBM-Ti64 samples, Figs. 4B–4D, exhibited fine lamellar microstructures (Widmanstätten morphology) consisting of α and β -phases. In these samples, the α -phase had an elongated needle-like grain structure, with the β -phase concentrated between these features. A detailed description of the microstructural characteristics of the present EBM-Ti64 samples is reported in a previous publication.¹²

While the microstructure of wrought-Ti64 was found to be homogenous across the entire surface, differences were observed along the build direction in the EBM-YZ samples. As shown in Fig. 4B, the microstructure corresponding to the starting point of the build exhibited a finer grain structure in comparison to the end of the build, Fig. 4C, which showed relatively coarsened features. The microstructure from sample EBM-XY, which is representative of the top view of a single layer, is presented in Fig. 4D. It showed a microstructure similar to that of the sample taken from the middle of sample EBM-YZ. Figure 5A presents an optical image of the etched EBM-YZ near the start of the build and Fig. 5B shows a high-magnification SEM micrograph of near the end of the build. The prior β -phase boundaries can be seen in Fig. 5A and are highlighted with yellow dashed lines in Fig. 5B. The columnar prior β -phase boundaries in EBM-Ti64 samples have been shown to have a strong $\langle 001 \rangle$ orientation along the build direction and are typically oriented along the build direction at an angle of $\sim 30^\circ$ – 40° .¹²

Bright-field TEM images of the XY plane microstructure from three different regions (the starting point, the middle, and the end) along the build direction, YZ plane, are shown in Fig. 6 and reveal a distinction. Several measurements of the width of α -lath were made on multiple TEM images using ImageJ software. At the starting point of the build, the needle-shaped α -platelets had an average width of 520 nm compared to the middle and end which exhibited average widths of 730 and 1240 nm, respectively. This demonstrated

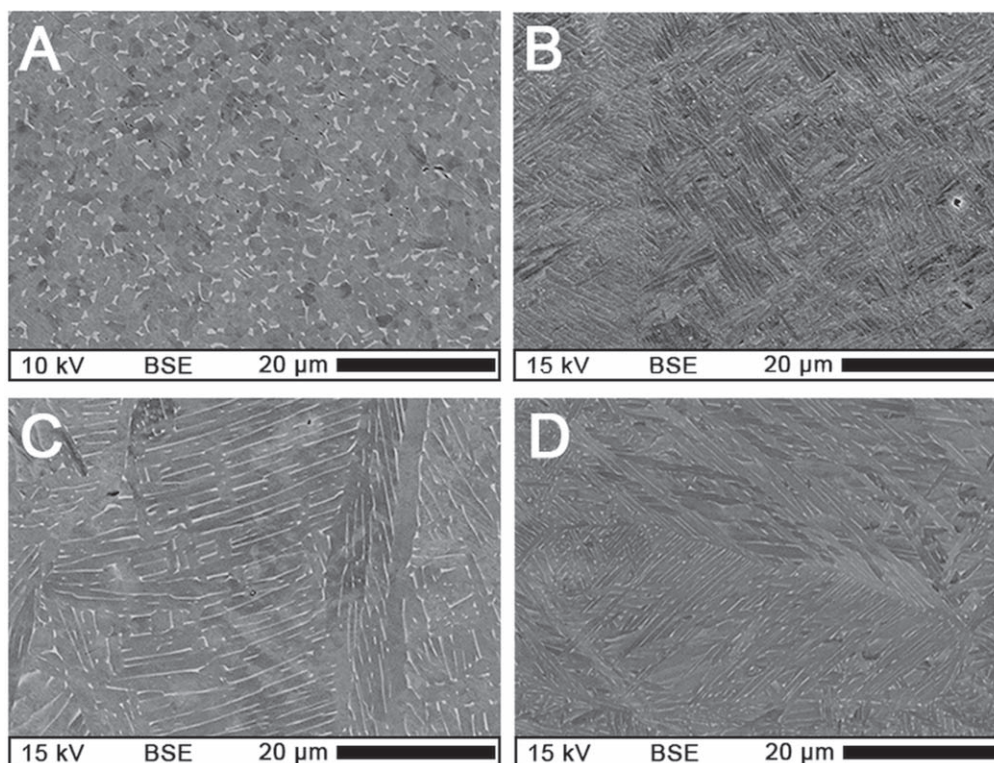


Figure 4. SEM Micrographs showing the microstructure of (A) wrought and (B-D) EBM Ti64. For the YZ plane, an image from the starting point (B) and the end (C) of the build are shown. The XY plane is shown in (D). The white phase is β and the dark, gray one is α .

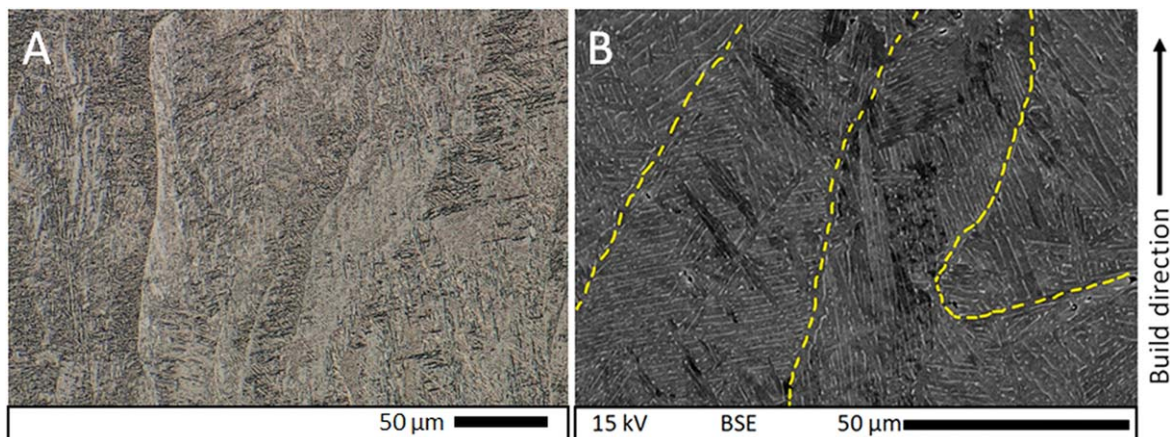


Figure 5. (A) Optical image of the etched YZ plane and (B) SEM micrograph of the YZ plane near the end of the build. β -boundaries can be seen in (A) and are highlighted with dashed yellow lines in (B).

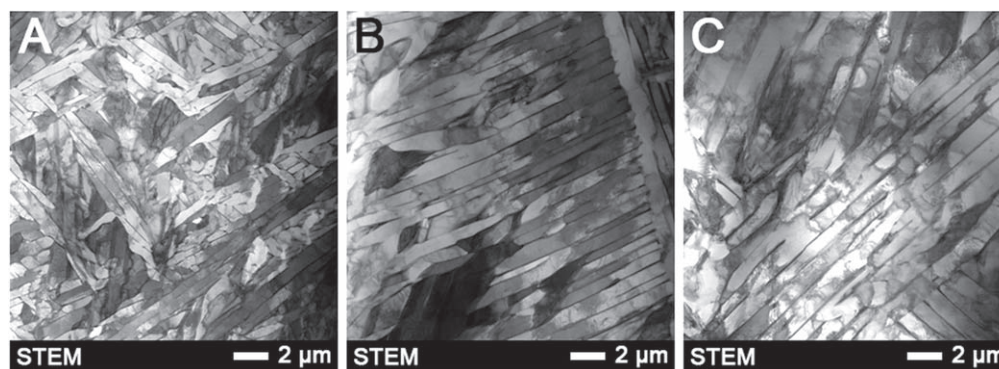


Figure 6. STEM images of EBM Ti64 samples, showing the starting point (A), the middle (B), and the end of the build (C).

a non-uniform microstructure along the YZ plane, which is parallel to the build direction, with a fine microstructure at the beginning of the build evolving to a coarser structure through the build. The finer microstructure at the beginning of the build is due to the faster cooling rates caused by the heat loss through the stainless steel build plate that can act as a heat sink. The rate of cooling in AM processes depends on three factors: (i) heat conduction through the underlying layers and build plate, (ii) heat conduction via powder-bed, and (iii) heat radiation from the scanned surface. The last two factors are not significant as the powder-bed is maintained at a high temperature (~ 650 °C) throughout the build under a vacuum atmosphere. It should be noted that the cylindrical rod in this study was printed in the horizontal orientation with a length of 120 mm. With increasing distance from the build plate, the heat input from each underlying layer results in a decrease in thermal gradients and cooling rates. Hence, a relatively coarser microstructure is obtained in the middle and end of the build.

In addition to microstructural changes, elemental distributions were also found to be affected by the relative location in the YZ plane. Elemental distribution maps collected using energy dispersive X-ray spectroscopy (EDS) in scanning TEM (STEM) are shown in Fig. 7. Semi-quantitative analyses from select locations at the starting point and the end of the build are summarized in Table III.

Inspection of these elemental distribution maps showed enrichment of Al and V in the α - and β -phases, respectively, with the concentration of V in the β -phase between 23.7 to 24.7 wt.% and that of Al in the α -phase between 5.5 to 5.9 wt.%. In addition, a measurable amount of Fe was found in the EBM samples. Inspection of the distribution maps indicated Fe existed dominantly in the β -phase as commonly observed in Fe-containing Ti alloys.

While the distribution of Al and V remained relatively unchanged along the build direction, close inspection of the Fe distribution maps showed a relatively high Fe content in the α -phase at the beginning of the build with segregation to the β -phase increasing towards the end. The semi-quantitative data in Table III suggest that Fe content in the α -phase decreased from 1.3 wt.% at the beginning to 0.2 wt.% at the end of the build. During the EBM process, although the powder-bed is maintained at 650 °C, the change in the distribution of Fe showed an increased influence of diffusion during later stages of the printing process.

The results from SEM-EDS analysis of wrought-Ti64 and EBM-YZ samples are summarised in Table IV. The analyses were performed on areas of $\sim 300 \times 500$ μm and compared to the EDS results from STEM, presented in Table III, provide more general information about the elemental composition of the samples. Based on the SEM/EDS results, the elemental compositions of the three areas along the build direction (the start, the middle, and the end of the build) in sample EBM-YZ were similar, showing a slightly lower concentration of Al compared to the wrought-Ti64 sample. The iron contents were similar in both the wrought and EBM-Ti64 samples.

Phase composition.—Selected area electron diffraction (SAED) performed in TEM on the EBM samples showed these samples contained α and β phases, no α' martensite was detected. The XRD patterns of the commercial wrought and EBM-Ti64 samples are presented in Fig. 8. All samples contained α -phase, with a hexagonal close-packed structure, and a small amount of β -phase, with a body-centred cubic (bcc) structure. Inspection of the wrought Ti64 sample XRD pattern, Fig. 8A, revealed that the (110) peak of the β -phase, the peak at a 2θ value of 39.7 degrees, was relatively more intense than those recorded on the EBM-produced samples.

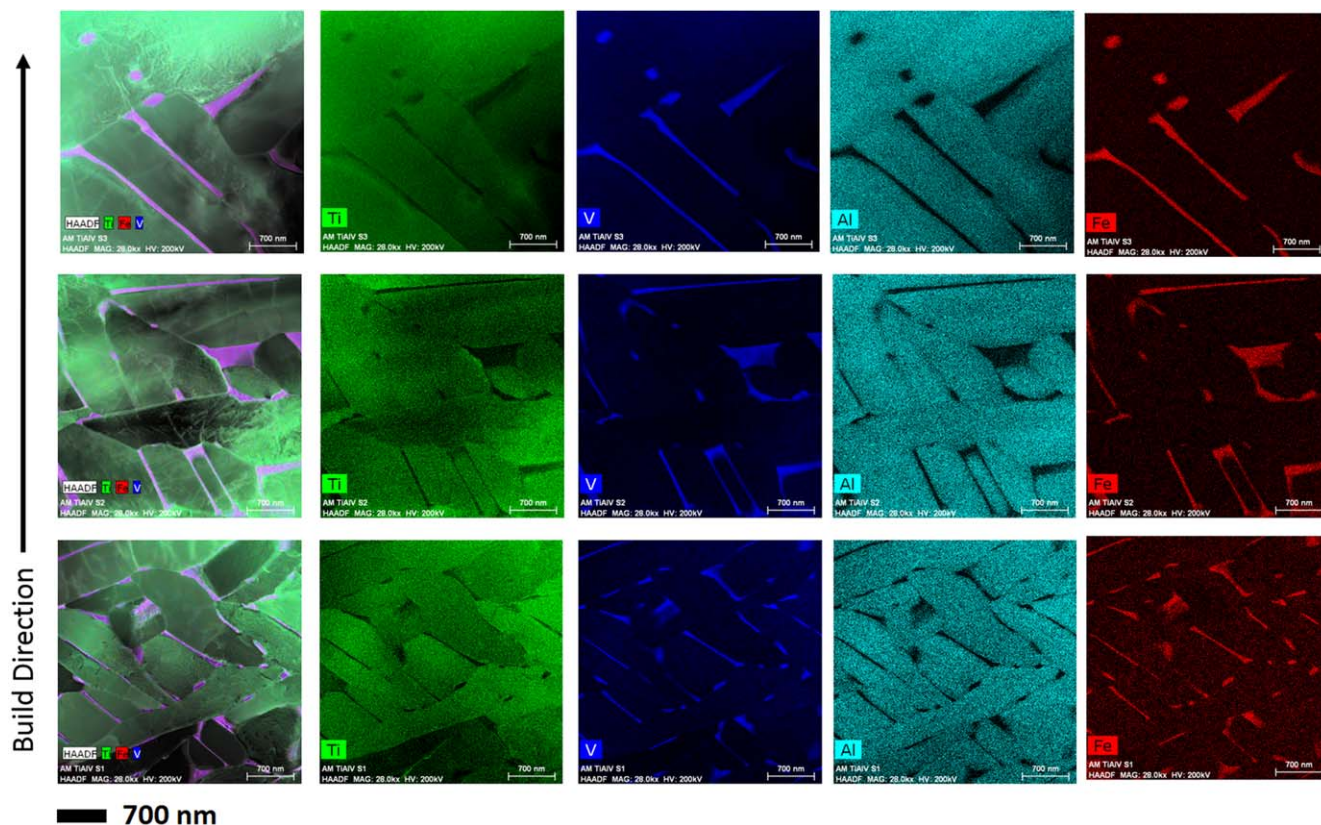


Figure 7. Elemental distribution maps acquired by EDS on TEM cross sections on EBM-Ti64 samples.

Table III. EDS analysis (STEM) of the α - and β -phase located at the starting point and the end of the build. Concentrations are reported as weight percentages.

Phase	Build Location	Ti	V	Fe	Al
α	Start	90.6	2.6	1.3	5.5
	End	91.9	2.1	0.2	5.9
β	Start	71.0	23.7	3.7	1.5
	End	70.7	24.7	3.2	2.7

Table IV. EDS analysis (SEM) of the wrought-Ti64 and EBM-YZ in three locations, the start, middle and end of the build. Concentrations are reported as weight percentages.

Sample	Build location	Ti	V	Fe	Al
Wrought-Ti64		89.5	4	0.2	6.4
EBM-YZ	Start	90.2	3.8	0.2	5.8
	Middle	90.3	3.8	0.2	5.7
	End	90.2	3.8	0.2	5.8

The XRD patterns collected from EBM-YZ sample at the starting point, the middle and the end of the build are compared in Fig. 8B. The integrated intensities of the (002) α and (101) α peaks at the starting point of the build were considerably less than those recorded at the end of the build. Another interesting observation to note was the increase in the integrated intensity of the (110) β peak in the build direction. At the starting point of the build, this peak was barely visible, while, at the end of the build it was very distinct. These results confirmed the SEM and TEM microstructural characterisation results. Based on the SEM micrographs, Figs. 4B and 4C, and

TEM images in Figs. 6 and 7, the β -phase grains were small and very fine at the beginning of the build, but increased in both length and width as the build progressed toward the end of the build direction. At the end of the build, the β -phase grains were very distinct, Fig. 4C. As shown by the EDS maps in Fig. 7 this was accompanied by the segregation of Fe into the β phase.

Corrosion behaviour.—On immersion in 3.5 wt.% NaCl solution, all specimens exhibited an upward trend in E_{corr} . A representative example of this trend, confirmed in a number (≥ 5) of repeat experiments, is shown in Fig. 9A. This upward trend with time suggested a slow oxidation of the surface which has not reached a steady-state condition after 12 h. Previously, Dai et al.²⁸ found E_{corr} continued to increase beyond 50 h for Ti64 produced by SLM. The minor fluctuations in E_{corr} , on the scale of a few mV, have also been observed previously,³⁵ but their origin remains unclear.

The properties of the surface oxides were investigated by EIS recorded at regular intervals (0.5, 2, 4, 8, 12 h) throughout the E_{corr} measurements. Examples of repeatedly measured ($n \geq 3$) Nyquist plots recorded on the XY plane of the EBM sample are shown in Fig. 9B. Similar measurements (not shown for brevity) on the YZ plane of the EBM sample and the wrought alloy exhibited similar trends. The EIS response was found to be dominated by a single capacitive loop, Bode plots of the same data showed no high frequency response which would not be visible in the Nyquist plots. An inability to observe a second impedance response at higher frequencies confirmed that the response of the alloy/oxide interface was not detectable and that the interfacial impedance was dominated by the relatively uniform properties of the oxide film.

The spectra were fitted to the single time constant circuit shown in Fig. 9A which was used previously by others^{36–38} although it should be noted that a two-time constant circuit was required to fit spectra recorded in more aggressive solutions when the oxide was possibly porous.^{28,39} In this circuit, R_s is the resistance of the solution which is effectively negligible and R_f is the resistance of the

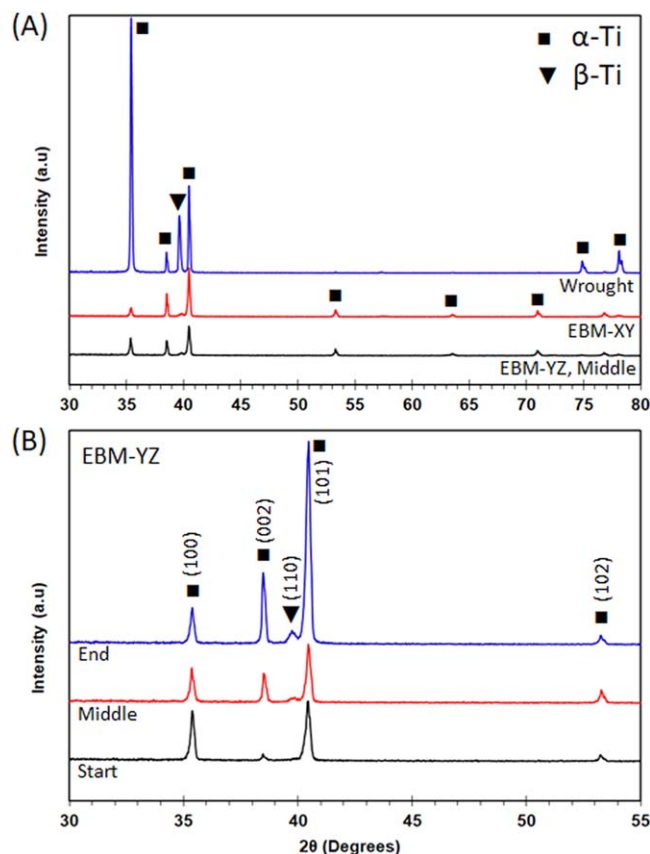


Figure 8. X-ray diffraction patterns of (A) the wrought, EBM-XY, and EBM-YZ (middle) samples, and (B) the YZ plane of the EBM sample at the starting point (S), the middle (M), and the end (E) of the build.

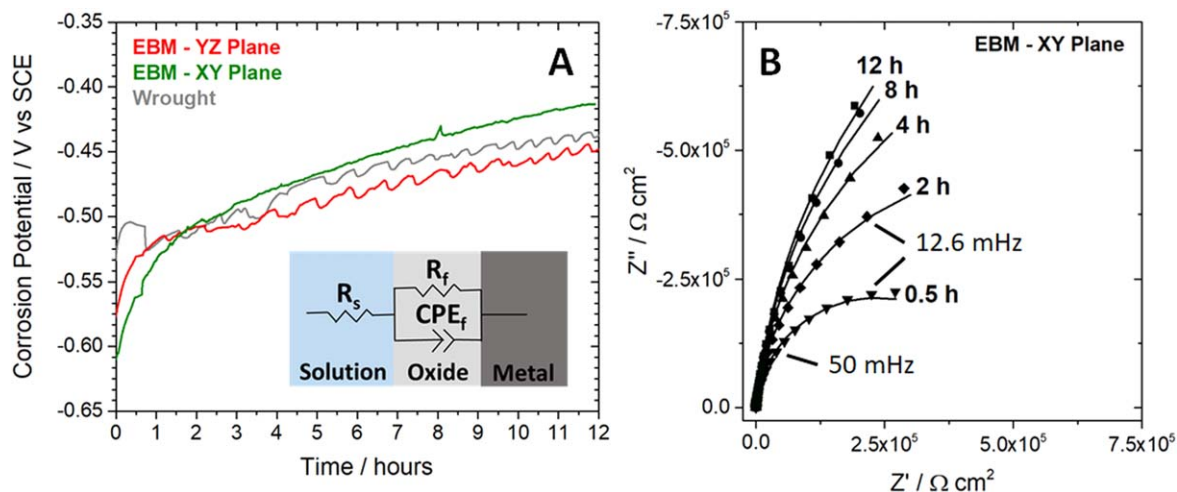


Figure 9. (A) Corrosion potential, E_{corr} , recorded in 3.5%wt. NaCl solution and (B) Nyquist plots collected by electrochemical impedance spectroscopy as a function of time during immersion. The equivalent circuit used to model experimental data is shown with a physical representation in (A). The experimental data are plotted as scatter plots and the fitted results are plotted with solid lines.

oxide film. To account for non-ideality in the capacitive response of the film, a constant phase element (CPE_f) was used to fit the spectra. Based on repeated experiments, R_f values obtained using the chi-squared test were consistently below 0.005. Examples of a fitted spectrum are shown by the lines in Fig. 9B. The average values of the circuit elements obtained from fits to the spectra are summarized in Table V.

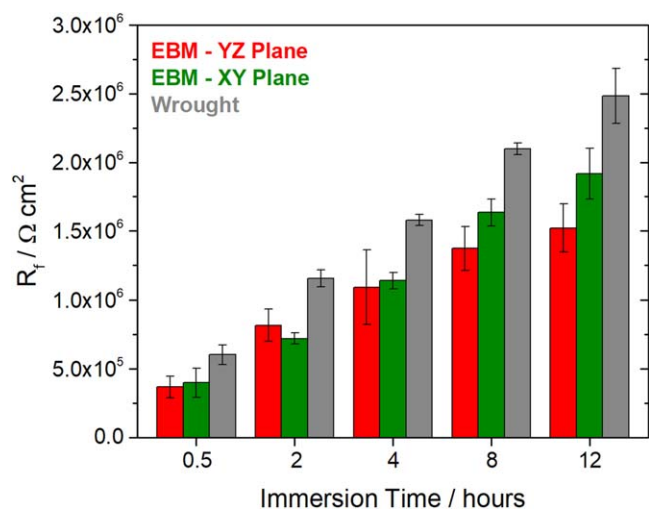
The R_f values obtained from the fitted spectra are plotted in Fig. 10 with the error bars indicating the sigma values obtained from

repeated measurements ($n \geq 3$). For all three specimens, R_f increased with exposure time consistent with the upward trends in E_{corr} with the high values indicating generally excellent passivity. These increases can be attributed to a slow improvement in the properties of the TiO₂ film as it thickened slightly as E_{corr} increased and the number density of point defects decreased.^{40,41} The lower R_f values for the EBM samples and their slower increase suggested the protective oxide on the wrought sample improved more readily with exposure time.

One possible explanation for the slightly lower performance of the EBM samples could be linked to the non-uniform distribution of alloying elements, namely Fe. The high Fe content in the segregated β -phase, which is more susceptible to corrosion than the α -phase,^{23,42} especially in areas near the end of the build in the EBM-YZ sample, could be an influential factor, although the effect was expected to be small at room temperature. In addition, the lower R_f values found on EBM samples may reflect the Widmanstätten microstructure, which has been shown to be more resistive to oxidation in comparison to the equiaxed microstructure found in the wrought alloy.⁴³ For the two EBM specimens, while the R_f values were approximately the same at short exposure times, the values for the XY plane continued to increase more rapidly at long times, more rapidly than those for the YZ plane. As discussed above, the microstructure of the XY plane was found to be most representative of the middle of the build suggesting this difference was a direct result of the microstructure found during the early stages of the build. However, since EIS yields a signal indicating only the averaged properties of the surface, it cannot yield information on whether this difference was due to compositional differences or the nature of the α/β phase boundaries which would be the most likely locations for differences in surface properties.²⁷ In order to study the local electrochemical properties and compare the corrosion behaviour of the early and later stages of the build, local electrochemical measurements such as scanning electrochemical microscopy (SECM) would provide useful information and are a subject of future work.

Table V. Average values of parameters obtained from fitted EIS plots (SD: standard deviation).

Samples	Immersion time (hr)	R_s ($\Omega \cdot \text{cm}^2$)	SD	CPE1-Q ($\mu\text{F cm}^{-2}$)	SD	CPE1-n	SD	R_f ($\Omega \cdot \text{cm}^2$)	SD
EBM-YZ	0.5	7.4	0.4	38.8	3.5	0.92	0.007	368×10^3	79×10^3
	2	7.5	0.4	36.5	3.1	0.92	0.006	817×10^3	119×10^3
	4	7.5	0.4	35.0	2.8	0.92	0.006	1092×10^3	269×10^3
	8	7.5	0.4	33.7	2.4	0.92	0.007	1374×10^3	159×10^3
	12	7.5	0.4	32.9	2.2	0.92	0.007	1522×10^3	174×10^3
EBM-XY	0.5	7.3	0.4	35.1	2.7	0.93	0.013	398×10^3	106×10^3
	2	7.4	0.4	31.1	2.1	0.93	0.011	720×10^3	41×10^3
	4	7.4	0.4	29.3	1.7	0.93	0.010	1141×10^3	61×10^3
	8	7.4	0.4	27.8	1.2	0.93	0.008	1634×10^3	97×10^3
	12	7.4	0.3	26.9	1.1	0.93	0.008	1917×10^3	185×10^3
Wrought	0.5	14.3	11.4	32.1	1.6	0.94	0.007	601×10^3	71×10^3
	2	13.8	10.5	31.6	1.3	0.94	0.007	1158×10^3	61×10^3
	4	16.1	14.4	31.1	1.0	0.94	0.006	1580×10^3	40×10^3
	8	14.4	11.6	30.1	0.7	0.94	0.006	2098×10^3	41×10^3
	12	14.9	12.1	29.4	0.8	0.94	0.005	2485×10^3	201×10^3

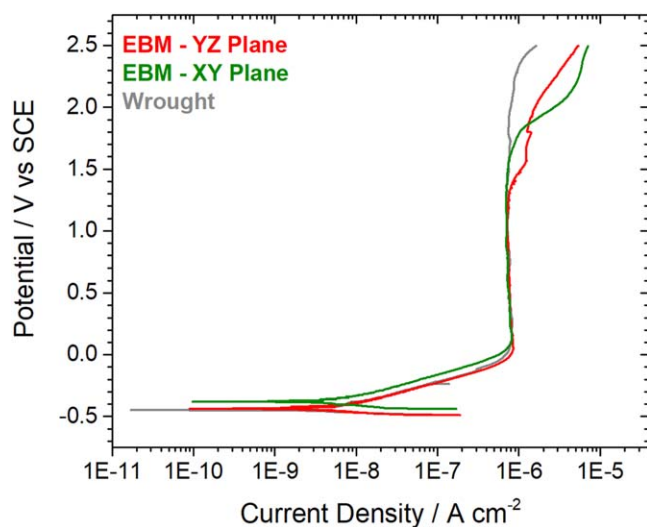
**Figure 10.** Average film resistance (R_f) as a function of immersion time for the Ti64 EBM 3D-YZ and 3D-XY samples as well as the wrought sample.

Grade-7 also shown to have homogeneously distributed Fe-containing β -phase along α -phase grain boundaries.⁴² When conditions were made more aggressive by raising the temperature, these β -phase intermetallics in Ti Grade-7 were shown to corrode preferentially compared to the α -grains.

The higher CPE values recorded on the EBM-YZ specimen suggested either the presence of a thinner oxide or a higher dielectric constant on this specimen. Since it is unlikely that significant differences in film thickness existed on the three specimens, especially on the α -grains, this would suggest that the larger CPE value could be attributed to a difference in the film dielectric constant, which would increase in the same order as the capacitance and would reflect an increase in defect density most likely at α/β phase boundaries.

At the conclusion of each immersion experiment (after 16 h), current-potential relationships were recorded using a linearly ramped applied potential. Representative data for the EBM-XY and EBM-YZ planes, as well as the wrought samples, are shown in Fig. 11. These plots exhibited a passive region stretching from ~ 0.0 V to ~ 1.2 V within which the current was the same for all specimens and $< 10^{-6}$ A cm^{-2} confirming passivity was maintained on all surfaces. Other studies³⁵ have reported higher current densities for Ti64 prepared by SLM when compared to the wrought alloy.

For the wrought alloy, the passive region extended to ~ 2.3 V. While the current increase at the anodic potential limit could be

**Figure 11.** Linear polarization curve recorded following a 16 h immersion in 3.5%wt. NaCl solution.

interpreted as the onset of pitting⁴⁴ this was not the case. The increased current can be attributed to valence band degeneracy leading to the oxidation of H_2O to O_2 as has been previously suggested.⁴⁵ The oxide on Ti and its alloys is a wide band gap (~ 3.0 V) n-type semiconductor with a flatband potential in neutral solution of ~ -0.4 V to -0.5 V⁴⁶ which would have led to such a degeneracy at a potential of ~ 2.3 V; i.e., around the potential at which the current increased on the wrought alloy, Fig. 11.

Both of the EBM specimens showed an increase in current at lower potentials than observed for the wrought alloy. This suggested the presence of interband defect states in both samples, in particular, the YZ plane which showed a current increase at a considerably lower potential than for the XY plane. This would be consistent with a higher defect density suggested by a higher dielectric constant for the EBM-YZ specimen as indicated by the EIS measurements. The most likely location of these defects was in the α/β phase boundaries though this cannot be confirmed in this study. That the current increases were not due to film breakdown leading to pit initiation was confirmed by the reverse potential scan from the anodic potential limit (not shown). On reversing the potential scan, the current density immediately decreased and did not exhibit the positive current hysteresis associated with the initiation of reactive pit sites. Similar behaviour has been previously noted.⁴⁵

Conclusions

The microstructural features and corrosion performance of Ti64 samples in the wrought condition were compared to samples prepared by EBM. The findings of this study can be summarized as:

- Samples prepared by EBM were found to contain a Widmanstätten structure in comparison to commercial wrought samples, which had a homogenous equiaxed grain structure.
- The microstructure of EBM samples was found to become coarser as a function of distance from the build base, where both α - and β -phase grains were found to be larger. Moreover, elemental distributions, mainly Fe-content, were also found to change as a function of distance from the build base. Increased segregation of Fe to the β -phase was observed along the build direction from the beginning to the end of the build.
- All samples showed similar passive corrosion behaviour with the wrought sample performing slightly better than samples prepared by EBM suggesting the difference in microstructure slightly affects the corrosion performance.
- The film resistance improved with exposure time faster on the wrought sample than on the YZ and XY planes of the EBM. This improvement can be attributed to a slight thickening of the surface oxide film accompanied by a decrease in number density of film defects (mainly O_V). For the EBM-XY and EBM-YZ samples, this improvement in passivity was slightly enhanced on the XY sample. The better performance of the wrought sample may be attributable to its uniform microstructure compared to the EBM samples, with the small difference in performance between the EBM samples possibly reflecting differences in the α/β phase boundaries in these samples.
- The EBM-YZ sample, which contained a gradient in both the size of α - and β -phase grains and segregation of the alloying elements in the build direction, showed a lower corrosion performance compared to EBM-XY and wrought-Ti64 samples. It appears that the difference in microstructure and distribution of elements along the build direction could influence the corrosion performance of EBM samples.

Acknowledgments

This work was supported by the Natural Sciences and Engineering Research Council of Canada (NSERC), grant number RGPIN-2016-04221, New Brunswick Innovation Foundation (NBIF), grant number RIF2017-071, and Atlantic Canada Opportunities Agency (ACOA)- project number 210414.

ORCID

V. Dehnavi  <https://orcid.org/0000-0002-8429-002X>
 J. D. Henderson  <https://orcid.org/0000-0001-7415-756X>
 C. Dharmendra  <https://orcid.org/0000-0002-1550-9219>

References

1. T. DebRoy, H. L. Wei, J. S. Zuback, T. Mukherjee, J. W. Elmer, J. O. Milewski, A. M. Beese, A. Wilson-Heid, A. De, and W. Zhang, "Additive manufacturing of metallic components—process, structure and properties." *Prog. Mater. Sci.*, **92**, 112 (2018).
2. G. Sander, J. Tan, P. Balan, O. Gharbi, D. R. Feenstra, L. Singer, S. Thomas, R. G. Kelly, J. R. Scully, and N. Birbilis, "Corrosion of additively manufactured alloys: a review." *Corrosion*, **74**, 1318 (2018).
3. W. E. Frazier, "Metal additive manufacturing: a review." *J. Mater. Eng. Perform.*, **23**, 1917 (2014).
4. J. J. Lewandowski and M. Seifi, "Metal additive manufacturing: a review of mechanical properties." *Annu. Rev. Mater. Res.*, **46**, 151 (2016).
5. S. Liu and Y. C. Shin, "Additive manufacturing of Ti6Al4V alloy: a review." *Mater. Des.*, **164**, 107552 (2019).
6. H. Shipley, D. McDonnell, M. Culleton, R. Coull, R. Lupoi, G. O'Donnell, and D. Trimble, "Optimisation of process parameters to address fundamental challenges during selective laser melting of Ti-6Al-4V: a review." *Int. J. Mach. Tools Manuf.*, **128**, 1 (2018).
7. C. Cui, B. M. Hu, L. Zhao, and S. Liu, "Titanium alloy production technology, market prospects and industry development." *Mater. Des.*, **32**, 1684 (2011).
8. P. Singh, H. Pungotra, and N. S. Kalsi, "On the characteristics of titanium alloys for the aircraft applications." *ICAAAM 2016 Materials Today: Proceedings*, **4**, 8971 (2017).
9. J. Alcisto et al., "Tensile properties and microstructures of laser-formed Ti-6Al-4V." *J. Mater. Eng. Perform.*, **20**, 203 (2011).
10. L. C. Zhang and H. Attar, "Selective laser melting of titanium alloys and titanium matrix composites for biomedical applications: a review." *Adv. Eng. Mater.*, **18**, 463 (2016).
11. S. L. Sing, J. An, W. Y. Yeong, and F. E. Wiria, "Laser and electron-beam powder-bed additive manufacturing of metallic implants: a review on processes, materials and designs." *J. Orthop. Res.*, **34**, 369 (2016).
12. C. Dharmendra, A. Hadadzadeh, B. S. Amirkhiz, A. Lloyd, and M. Mohammadi, "Deformation mechanism and fracture of electron beam melted Ti-6Al-4V." *Mater. Sci. Eng. A Struct. Mater. Prop. Microstruct. Process.*, **771**, 1 (2020).
13. M. Koike, P. Greer, K. Owen, G. Lilly, L. E. Murr, S. M. Gaytan, E. Martinez, and T. Okabe, "Evaluation of titanium alloys fabricated using rapid prototyping technologies-electron beam melting and laser beam melting." *Materials (Basel)*, **4**, 1776 (2011).
14. C. Dharmendra, R. Alaghmandfar, A. Hadadzadeh, B. S. Amirkhiz, and M. Mohammadi, "Influence of build orientation on small-scale properties of electron beam melted Ti-6Al-4V." *Mater. Lett.*, **266**, 126970 (2019).
15. B. Wysocki, P. Maj, A. Krawczyńska, K. Roźniatowski, J. Zdunek, K. J. Kurzydłowski, and W. Świąszkowski, "Microstructure and mechanical properties investigation of CP titanium processed by selective laser melting (SLM)." *J. Mater. Process. Technol.*, **241**, 13 (2017).
16. S. S. Al-Bermani, M. L. Blackmore, W. Zhang, and I. Todd, "The origin of microstructural diversity, texture, and mechanical properties in electron beam melted Ti-6Al-4V." *Metall. Mater. Trans. A Phys. Metall. Mater. Sci.*, **41**, 3422 (2010).
17. Y. R. Choi, S. D. Sun, Q. Liu, M. Brandt, and M. Qian, "Influence of deposition strategy on the microstructure and fatigue properties of laser metal deposited Ti-6Al-4V powder on Ti-6Al-4V substrate." *Int. J. Fatigue*, **130**, 1 (2020).
18. Y. Y. Sun, S. Gulizia, C. H. Oh, D. Fraser, M. Leary, Y. F. Yang, and M. Qian, "The influence of as-built surface conditions on mechanical properties of Ti-6Al-4V additively manufactured by selective electron beam melting." *JOM*, **68**, 791 (2016).
19. L. E. Murr et al., "Microstructures and mechanical properties of electron beam-rapid manufactured Ti-6Al-4V biomedical prototypes compared to wrought Ti-6Al-4V." *Mater. Charact.*, **60**, 96 (2009).
20. E. Uhlmann, R. Kersting, T. B. Klein, M. F. Cruz, and A. V. Borille, "Additive manufacturing of titanium alloy for aircraft components." *Procedia CIRP* (Elsevier B.V) 15th Machining Innovations Conference for Aerospace Industry, **35**, 55 (2015).
21. M. Ask, J. Lausmaa, and B. Kasemo, "Preparation and surface spectroscopic characterization of oxide films on Ti6Al4V." *Appl. Surf. Sci.*, **35**, 283 (1989).
22. M. Ask, U. Rolander, J. Lausmaa, and B. Kasemo, "Microstructure and morphology of surface oxide films on Ti-6Al-4V." *J. Mater. Res.*, **5**, 1662 (1990).
23. X. He, J. J. Noël, and D. W. Shoesmith, "Effects of iron content on microstructure and crevice corrosion of grade-2 titanium." *Corrosion*, **60**, 378 (2004).
24. Y. J. Kim and R. A. Oriani, "Brine radiolysis and its effect on the corrosion of grade 12 titanium." *Corrosion*, **43**, 92 (1987).
25. Y. J. Kim and R. A. Oriani, "Corrosion properties of the oxide film formed on grade 12 titanium in brine under gamma radiation." *Corrosion*, **43**, 85 (1987).
26. D. W. Shoesmith and J. J. Noël, "Corrosion of Titanium and Its Alloys." *Shreir's Corrosion* (Elsevier, Amsterdam) **3**, 2042 (2010).
27. R. Zhu, Z. Qin, J. J. Noël, D. W. Shoesmith, and Z. Ding, "Analyzing the influence of alloying elements and impurities on the localized reactivity of titanium grade-7 by scanning electrochemical microscopy." *Anal. Chem.*, **80**, 1437 (2008).
28. N. Dai, L. C. Zhang, J. Zhang, X. Zhang, Q. Ni, Y. Chen, M. Wu, and C. Yang, "Distinction in corrosion resistance of selective laser melted Ti-6Al-4V alloy on different planes." *Corros. Sci.*, **111**, 703 (2016).
29. Y. Bai, X. Gai, S. Li, L. C. Zhang, Y. Liu, Y. Hao, X. Zhang, R. Yang, and Y. Gao, "Improved corrosion behaviour of electron beam melted Ti-6Al-4V alloy in phosphate buffered saline." *Corros. Sci.*, **123**, 289 (2017).
30. L. E. Murr, S. M. Gaytan, D. A. Ramirez, E. Martinez, J. Hernandez, K. N. Amato, P. W. Shindo, F. R. Medina, and R. B. Wicker, "Metal fabrication by additive manufacturing using laser and electron beam melting technologies." *J. Mater. Technol.*, **28**, 1 (2012).
31. S. Shamsdini, S. Shakerin, A. Hadadzadeh, B. S. Amirkhiz, and M. Mohammadi, "A trade-off between powder layer thickness and mechanical properties in additively manufactured maraging steels." *Mater. Sci. Eng. A*, **776**, 1 (2020).
32. C. J. Todaro, M. A. Easton, D. Qiu, D. Zhang, M. J. Birmingham, E. W. Lui, M. Brandt, D. H. StJohn, and M. Qian, "Grain structure control during metal 3D printing by high-intensity ultrasound." *Nat. Commun.*, **11**, 1 (2020).
33. A. Safdar, L. Y. Wei, A. Snis, and Z. Lai, "Evaluation of microstructural development in electron beam melted Ti-6Al-4V." *Mater. Charact.*, **65**, 8 (2012).
34. C. de Formanoir, S. Michotte, O. Rigo, L. Germain, and S. Godet, "Electron beam melted Ti-6Al-4V: Microstructure, texture and mechanical behavior of the as-built and heat-treated material." *Mater. Sci. Eng. A*, **652**, 105 (2016).
35. N. Dai, L. C. Zhang, J. Zhang, Q. Chen, and M. Wu, "Corrosion behavior of selective laser melted Ti-6Al-4 V alloy in NaCl solution." *Corros. Sci.*, **102**, 484 (2016).
36. X. Gong, Y. Cui, D. Wei, B. Liu, R. Liu, Y. Nie, and Y. Li, "Building direction dependence of corrosion resistance property of Ti-6Al-4V alloy fabricated by electron beam melting." *Corros. Sci.*, **127**, 101 (2017).

37. D.-I. Seo and J.-B. Lee, "Corrosion characteristics of additive-manufactured Ti-6Al-4V using microdroplet cell and critical pitting temperature techniques." *J. Electrochem. Soc.*, **166**, C428 (2019).
38. B. Zhao, H. Wang, N. Qiao, C. Wang, and M. Hu, "Corrosion resistance characteristics of a Ti-6Al-4V alloy scaffold that is fabricated by electron beam melting and selective laser melting for implantation in vivo." *Mater. Sci. Eng. C*, **70**, 832 (2017).
39. S. Tamilselvi, V. Raman, and N. Rajendran, "Corrosion behaviour of Ti-6Al-7Nb and Ti-6Al-4V ELI alloys in the simulated body fluid solution by electrochemical impedance spectroscopy." *Electrochim. Acta*, **52**, 839 (2006).
40. R. M. Torresi, O. R. Cámara, C. P. De Pauli, and M. C. Giordano, "Hydrogen evolution reaction on anodic titanium oxide films." *Electrochim. Acta*, **32**, 1291 (1987).
41. C. da Fonseca, S. Boudin, and M. da Cunha Belo, "Characterisation of titanium passivation films by in situ ac impedance measurements and XPS analysis." *J. Electroanal. Chem.*, **379**, 173 (1994).
42. X. He, J. J. Noël, and D. W. Shoesmith, "Temperature effects on oxide film properties of grade-7 titanium." *Corrosion*, **63**, 781 (2007).
43. T. Sugahara, D. A. P. Reis, C. Moura Neto, M. J. R. Barboza, E. A. C. Perez, F. Piorino Neto, and A. C. O. Hirschmann, "The effect of Widmanstätten and equiaxed microstructures of Ti-6Al-4V on the oxidation rate and creep behavior." *Materials Science Forum*, **636-637**, 657 (2010).
44. F. A. Posey and E. G. Bohlmann, "Pitting of titanium alloys in saline waters." *Desalination*, **3**, 269 (1967).
45. F. Hua, K. Mon, P. Pasupathi, G. Gordon, and D. Shoesmith, "A review of corrosion of titanium grade 7 and other titanium alloys in nuclear waste repository environments." *Corrosion*, **61**, 987 (2005).
46. J. Pan, D. Thierry, and C. Leygraf, "Electrochemical and XPS studies of titanium for biomaterial applications with respect to the effect of hydrogen peroxide." *J. Biomed. Mater. Res.*, **28**, 113 (1994).